

## Chirality Transfer

# Unraveling the Chirality Transfer from Circularly Polarized Light to Single Plasmonic Nanoparticles

Seunghoon Lee<sup>†,\*</sup>, Chenghao Fan<sup>†</sup>, Artur Movsesyan, Johannes Bürger, Fedja J. Wendisch, Leonardo de S. Menezes, Stefan A. Maier, Haoran Ren, Tim Liedl, Lucas V. Besteiro, Alexander O. Govorov,<sup>\*</sup> and Emiliano Cortés<sup>\*</sup>

**Abstract:** Due to their broken symmetry, chiral plasmonic nanostructures have unique optical properties and numerous applications. However, there is still a lack of comprehension regarding how chirality transfer occurs between circularly polarized light (CPL) and these structures. Here, we thoroughly investigate the plasmon-assisted growth of chiral nanoparticles from achiral Au nanocubes (AuNCs) via CPL without the involvement of any chiral molecule stimulators. We identify the structural chirality of our synthesized chiral plasmonic nanostructures using circular differential scattering (CDS) spectroscopy, which is correlated with scanning electron microscopy imaging at both the single-particle and ensemble levels. Theoretical simulations, including hot-electron surface maps, reveal that the plasmon-induced chirality transfer is mediated by the asymmetric distribution of hot electrons on achiral AuNCs under CPL excitation. Furthermore, we shed light on how this plasmon-induced chirality transfer can also be utilized for chiral growth in bimetallic systems, such as Ag or Pd on AuNCs. The results presented here uncover fundamental aspects of chiral light-matter interaction and have implications for the future design and optimization of chiral sensors and chiral catalysis, among others.

## Introduction

Chirality, the geometrical concept describing one object is non-superimposable on its mirror image, plays a crucial role in biology and chemistry.<sup>[1–3]</sup> The interaction of chiral matter

with circularly polarized light (CPL), known as the chiroptical property, is essential for exploring and manifesting chirality.<sup>[4–6]</sup> However, the utilization of chiroptical properties for chiral organic molecules is limited by the inherently weak light-matter interaction, which arises from their small

[\*] Prof. Dr. S. Lee,<sup>†</sup> C. Fan,<sup>†</sup> J. Bürger, Dr. F. J. Wendisch, Prof. Dr. L. de S. Menezes, Prof. Dr. S. A. Maier, Prof. Dr. E. Cortés  
Chair in Hybrid Nanosystems, Nanoinstitute Munich, Faculty of Physics, Ludwig-Maximilians-Universität München  
80539 München (Germany)  
E-mail: emiliano.cortes@lmu.de

Prof. Dr. S. Lee<sup>†</sup>  
Department of Chemistry, Dong-A University  
Busan, 49315 (South Korea)  
E-mail: seunghoon@dau.ac.kr

Prof. Dr. S. Lee<sup>†</sup>  
Department of Chemical Engineering (BK21 FOUR Graduate Program), Dong-A University  
Busan, 49315 (South Korea)

Dr. A. Movsesyan, Prof. Dr. A. O. Govorov  
Department of Physics and Astronomy, Ohio University  
Athens, Ohio 45701 (United States)  
E-mail: govorov@ohio.edu

Prof. Dr. A. O. Govorov  
Nanoscale and Quantum Phenomena Institute, Ohio University  
Athens, Ohio 45701 (United States)

Dr. A. Movsesyan  
Institute of Fundamental and Frontier Sciences, University of Electronic Science and Technology of China  
Chengdu 610054 (P. R. China)

Prof. Dr. L. de S. Menezes  
Departamento de Física, Universidade Federal de Pernambuco  
50670-901 Recife-PE (Brazil)

Prof. Dr. L. de S. Menezes  
Faculty of Physics and Center for Nanoscience, Ludwig-Maximilians-University München  
80539 München (Germany)

Prof. Dr. S. A. Maier, Dr. H. Ren  
School of Physics and Astronomy, Monash University  
Clayton, Victoria 3800 (Australia)

Prof. Dr. S. A. Maier  
The Blackett Laboratory, Imperial College London  
London SW7 2AZ (United Kingdom)

Prof. Dr. T. Liedl  
Department of Physics and Center for NanoScience, Ludwig-Maximilians-Universität München  
Amalienstrasse 54, 80799 München (Germany)

Dr. L. V. Besteiro  
CINBIO, University of Vigo  
36310 Vigo (Spain)

[†] These authors contributed equally to this work.

© 2024 The Authors. Angewandte Chemie International Edition published by Wiley-VCH GmbH. This is an open access article under the terms of the Creative Commons Attribution License, which permits use, distribution and reproduction in any medium, provided the original work is properly cited.

size and, consequently, small optical cross-sections relative to the wavelength of light.<sup>[7–8]</sup> Recently, chiral plasmonic nanostructures have drawn tremendous interest due to their unique ability to enhance chiroptical properties based on localized surface plasmon resonance (LSPR), leading to various potential applications in fields such as photonics, asymmetric catalysis, enantioselective separation, chiroptical sensing, and chiral plasmonic devices.<sup>[4,8–27]</sup> Moreover, studying the evolution of chiral plasmonic nanostructures, which exhibit distinctive chiroptical responses, could provide new tools for investigating the origin of life and the asymmetric properties of matter.<sup>[2–3]</sup>

Chirality transfer from a chiral entity to an achiral entity can occur via Coulomb interactions (dipole and multipole), such as those between non-chiral nanocrystals and chiral molecular complexes;<sup>[4,28–31]</sup> the growth of chiral plasmonic seeds under the stimulation of chiral molecules;<sup>[12,32–37]</sup> or the formation of chiral nanostructures influenced by the plasmonic coupling between CPL and matter.<sup>[19,38–41]</sup> Chirality transfer has the potential to drive enantioselective chemical reactions, help construct chiral nanostructures with unique chiral optical properties and enable their applications.<sup>[4,8–27]</sup> In this regard, there have been numerous efforts to understand the underlying mechanisms in chirality transfer and to develop chiral plasmonic nanostructures to enhance such effects.<sup>[19,38–41]</sup> Despite the remarkable achievements on the synthesis of chiral plasmonic nanoparticles through chirality transfer, some deficiencies in previous studies still impede a clear comprehension of plasmon-induced chirality transfer and the fabrication of better chiral plasmonic nanostructures. For instance, chiral light-matter interactions can be partially counteracted by the free three-dimensional rotations of nanoparticles during their growth in solutions, thus reducing their final structural chirality.<sup>[19,38,40,42]</sup> In addition, the presence of chiral molecules in the synthesis can stimulate molecule-induced chirality transfer, complexing the research system.<sup>[19,40–41]</sup>

To settle these problems, it is necessary to design a chirality transfer experiment with controlled chiral entities. Here, we systematically investigate a plasmon-driven synthesis for chiral growth of nanoparticles via illumination of achiral nanoparticles with CPL without any chiral molecule stimulators. We use Au nanocubes (AuNCs), stabilized by achiral ligands,<sup>[43]</sup> as seeds for preparing chiral nanostructures. The chiral nanoparticles are synthesized under CPL in the presence of Au<sup>3+</sup> thus inducing chiral growth by hot electrons (HEs) with chiral distributions on the surface of the AuNCs, and methanol (MeOH) serves as a hole scavenger. Both left (L) and right (R) AuNCs enantiomers (LAuNCs and RAuNCs, respectively) are successfully synthesized with left- and right-circularly polarized (LCP and RCP) light. To investigate the chiroptical properties of the obtained chiral nanostructures, we utilize single-particle circular differential scattering (CDS) spectroscopy, which allows us to correlate the chiroptical properties of our nanostructures with theoretical calculations modeling the spatial distribution of hot-carriers in single AuNCs.<sup>[4–6]</sup> Also, to accurately determine the chirality-transfer mechanism, it is pivotal to move beyond ensemble measurements, as the

structure–performance relation needs to be determined, and as such single-particle measurements are expedient. CDS spectroscopy reveals that the synthesized AuNCs illuminated with CPL exhibited intrinsic chiroptical properties, while their counterparts (UAuNCs) grown under unpolarized (UP) light did not elicit such properties. Through computational models, we illustrate the microscopic character of the chirality transfer mechanism from light to matter and use them to attribute this role to the chiral distribution of HEs in the AuNCs, which promotes plasmon-induced chemical reactions driving the entire particle system towards a specific chirality. Our experimental measurements and theoretical simulations clarify this plasmon-induced chirality transfer mechanism, which enables the fabrication of chiral plasmonic nanostructures without the engagement of chiral molecules.

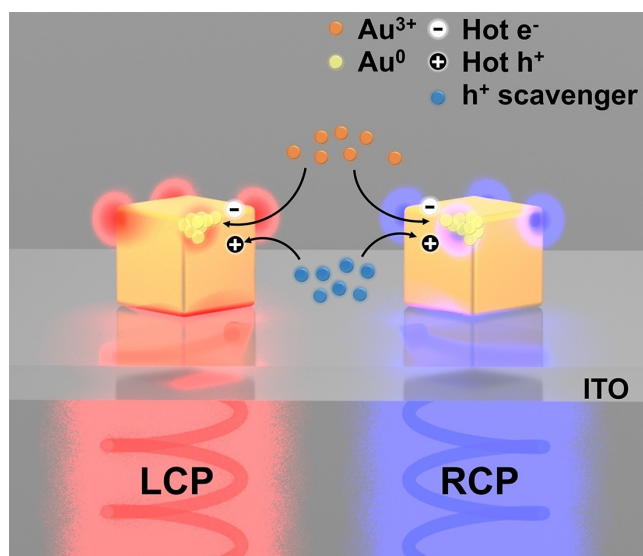
Noteworthy, this plasmon-induced chirality transfer can also occur for the growth of other metals on AuNCs. This prompts us to implement hybrid chiral plasmonic nanomaterials, which can facilitate enhanced enantioselective recognition, chiroplasmonic sensing, and polarization-dependent photochemistry.<sup>[44–46]</sup> We explore the chiral growth of Ag and Pd on AuNCs, and both present chiral morphologies and clear chiroptical properties, highlighting the wide applicability of this chiral synthesis method.

## Results and Discussion

### Plasmon-Directed Growth of Chiral Au Nanostructures

To examine the chirality transfer between CPL and matter, we developed a plasmon-driven synthesis of chiral Au nanostructures. Our procedure, based on the plasmon-driven nanoparticle growth process by HE-mediated reduction reactions,<sup>[19,40–41,47–48]</sup> was intentionally designed to unravel the plasmon excitation effect during the chirality transfer. In a typical synthesis, achiral AuNCs seeds with an average length of 75 nm, which were synthesized using a previously reported method,<sup>[43]</sup> were adsorbed onto an indium tin oxide (ITO) coated glass slide (Scheme 1, Figure 1a, Figure S1). To synthesize chiral Au nanostructures, we prepared an aqueous solution containing HAuCl<sub>4</sub>, MeOH, and Polyvinylpyrrolidone (PVP, the capping agent and stabilizer) as a growth solution, then illuminated the substrate with CPL generated with laser light at a wavelength of 600 nm. In the photochemical growth mechanism, PVP adsorbed on the Au surface can prolong the hot-electron lifetime and promote the multi-electron reduction of HAuCl<sub>4</sub> with slow kinetics, and MeOH can scavenge the hot holes.<sup>[48]</sup>

Unlike previous strategies for asymmetric photo-mediated synthesis - which were based on molecular-induced chirality transfer<sup>[19,40–41]</sup> - we conducted the reactions without any chiral molecules to clarify the origin of chirality transfer. The reactions were also performed on a substrate rather than in a colloidal solution, in order to spatially resolve the interaction between the incident CPL and the plasmonic nanoparticles. We achieved this by fixing the



**Scheme 1.** Schematic illustration for the plasmon-induced chiral growth from an achiral AuNC. Depending on the LCP and RCP illumination, AuNCs on the ITO substrate exhibit different hot electron generation surface profiles to induce local growth. In the local growth, hot electrons reduce Au<sup>3+</sup> ion to Au<sup>0</sup> metal, and hot holes are consumed by hole scavenger (methanol in our system).

orientation of the nanoparticles during growth.<sup>[49]</sup> The growth solution was left undisturbed on the ITO plate in a room temperature reactor, subsequently, the samples were exposed to illumination for 20 minutes (Scheme 1, see Supporting Information S1.3 & S1.4 for more experimental details). Scanning electron microscopy (SEM) images of the products clearly confirm the inherent asymmetric morphology of the synthesized nanostructures with average particle sizes of (150 ± 8) nm, (152 ± 6) nm, and (126 ± 8) nm for UP, RCP, and LCP illumination, respectively (Figure 1b–d, Figure S2).

To prove that this asymmetric growth is based on chirality transfer from CPL, we measured the optical properties of each nanostructure with a home-made single-particle CDS spectroscopy setup (Figure S3, see Supporting Information S1.5 for more experimental details), which in contrast to ensemble techniques, allows for the correlation between SEM images and chiroptical responses of individual structures.<sup>[4–5,12]</sup> Furthermore, performing single-particle level analysis can improve our understanding of the mechanism and strength of light-matter interactions in this system. Up to now, many researchers have reported on the use of single-particle spectroscopy to improve the sensitivity and detection limit of chiral sensing.<sup>[4–5,50–53]</sup> Despite these advantages, a few artifacts could occur in the measurement of single-particle CDS spectroscopy, such as the orientation of nanostructures relative to the axes of the CPL and also strong linear dichroism interfering with the circular dichroism (CD) signal if the input beam is slightly elliptical.<sup>[5,52]</sup> To assess these potential artifacts in our measurements, we measured both single-particle (red dotted areas) and ensemble (yellow dotted area) scattering to compare the optical properties of each nanoparticle (Figure 1e). Taken

together, ensemble averaging can eliminate statistical artifacts during CDS measurements, though it would also average out the interesting features of single-particle optical properties.

Interestingly, each nanoparticle displayed intrinsic optical properties that were strongly correlated with the polarization of illuminated light during growth. We observed that the synthesized AuNCs grown under CPL exhibited intrinsic chiroptical performance. The maximum LSPR peak of LAuNCs, RAuNCs, and UAuNCs appeared at 657, 692, and 730 nm, respectively, and the peak position of each NC was red-shifted compared to the one at 590 nm for achiral AuNCs (Figure 1f). The redshift of the LSPR peak is well explained by the increasing size of the particles during growth.<sup>[54]</sup> Single-particle CDS indicates that LAuNCs and RAuNCs, when illuminated with left- and right-circularly polarized photons, exhibit negative and positive CDS signals in the visible range, respectively. In contrast, AuNCs and UAuNCs exhibited low and irregular chiroptical activities in CDS measurements, suggesting their lack of structural chirality (Figure 1g, Figure S4 and 5). Based on the AuNC CDS measurements, the other CDS values lower than AuNCs could be ignored, considering that AuNCs are expected to show achiral properties and such results may be attributed to measurement error. Additionally, we clarified the weak chiroptical activity of UAuNCs through simulation (Figure S8). The weak chirality of UAuNCs was induced by the random clusters formation and growth on AuNCs, where the symmetry cancels out, resulting in low chirality. These chiroptical responses of each NC were also well reproduced in the ensemble scattering measurements (Figure 1h–i), confirming the accuracy of our results obtained from the single-particle analysis. The synthesized LAuNCs and RAuNCs exhibited complex shapes in the SEM images; nevertheless, they did display preferred handedness based on their CDS, with positive for RAuNCs and negative for LAuNCs (Figure S4, 6, and 7), which suggests the existence of localized photochemical reactions that enable chirality transfer. To further confirm the chiral morphology of our nanoparticles, we performed rotated and tilted SEM characterizations of a representative single particle (Figure S9).

#### Theoretical Calculations of Polarization-Dependent Plasmonic Properties of Au Nanocubes

To interpret in detail how this chirality transfer occurs, we calculated the absorption, scattering, and HE generation rate spectra of achiral AuNCs using COMSOL simulations (see Supporting Information S1.6 for further details on the calculations). The theoretical model of the AuNC was built with an edge length of 75 nm, corresponding to its experimentally observed size (Figure 2a and Figure S1). First, to validate our single-particle dark field scattering measurements are well-established, we simulated the absorption and scattering of AuNCs on ITO plates in air (Figure 2b). The theoretical scattering peak position of the AuNCs was placed at 596 nm, which is in very good accordance with the experimental scattering peak position (590 nm) observed in

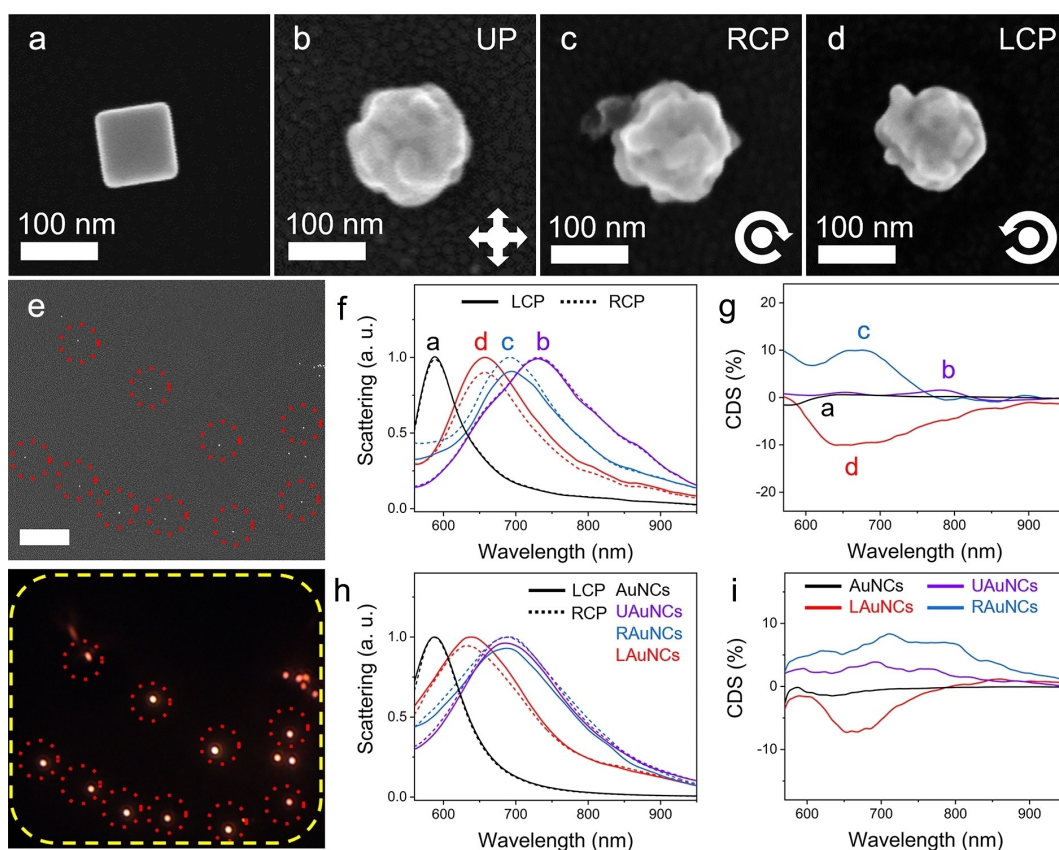


**Figure 1.** Characterization of plasmon-induced chiral growth of AuNCs. (a–d) Representative SEM images of AuNC (gold nanocubes before growth); UAuNC, RAuNC, and LAuNC (gold nanocubes after growth under UP, RCP, and LCP illumination). (e) Correlated SEM image (upper panel) and dark-field scattering image (lower panel) for single-particle CD scattering measurements (red dotted areas) and for ensemble CD scattering measurements (yellow dotted area). The inset scale bar indicates 10  $\mu\text{m}$ . (f–i) Normalized CD scattering spectra (solid line, LCP; dashed line, RCP) and differential CD scattering (CDS) spectra of different NPs are shown. (f–g) The corresponding single-particle spectra of each NC displayed in (a–d) and (h–i) the ensemble spectra of each NC are shown.

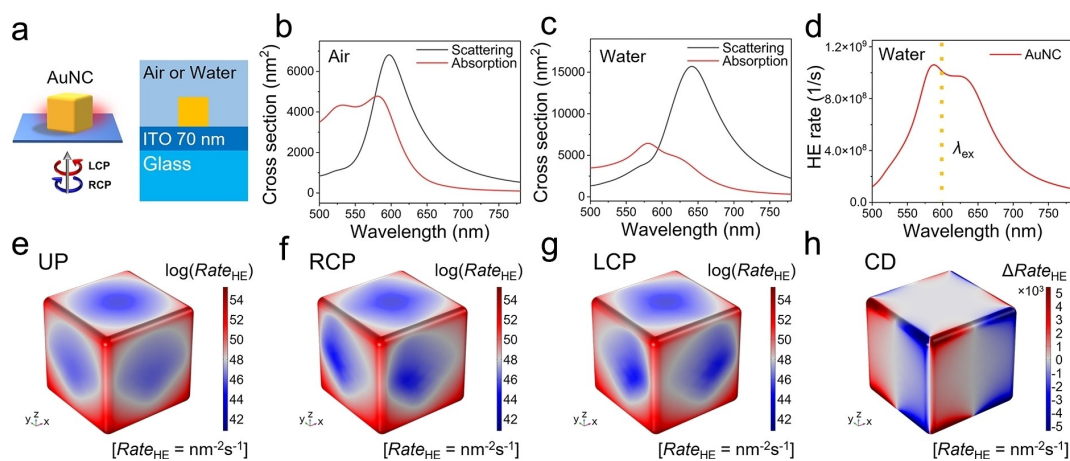


**Figure 2.** Theoretical optical properties and polarization-dependent HE generation rates of an AuNC. (a) Schematic illustration of theoretical simulation model for characterizing the optical properties of a 75 nm-sized AuNC. Calculated absorption and scattering spectra of a model AuNC in (b) air and (c) water. (d) Calculated wavelength-dependent HE generation rate spectrum of AuNC. The excitation wavelength  $\lambda_{\text{ex}}$  used in the experiments is shown as a yellow dotted line. (e–g) Surface maps showing HE generation rates on a log scale for a model AuNC in water under (e) UP, (f) RCP, and (g) LCP illumination, respectively. (h) Calculated surface CD map for differential HE rates of AuNC between RCP and LCP. The excitation wavelength ( $\lambda_{\text{ex}}$ ) for HE surface maps (e–h) is 600 nm.

our single-AuNC dark-field scattering measurements (Figure 1f).

Next, to study local photochemistry at the surfaces of AuNCs, we simulated the plasmonic properties of achiral AuNCs in water. This environment is analogous to the conditions for our photochemical reactions. As shown in Figure 2c, the main LSPR peak red-shifted when compared to the air condition as the refractive index of the surrounding dielectric medium increased.<sup>[55]</sup> The computed absorption spectrum of the AuNC manifests two absorption bands (Figure 2c), indicating the excitation of dipolar and higher-order plasmon modes. We understand the physical process of chiral growth as driven by a hot carrier injection mechanism, enabled by the strong electric field at the NC's surface due to its plasmonic resonance.<sup>[42,56]</sup> The HE generation rate spectrum reflects these two plasmon bands as well (Figure 2d). To unveil the mechanism of chiral growth, we further map the spatial distribution of HE generation rates depending on the state of polarization of light at 600 nm excitation, the wavelength we chose to drive the plasmon-induced chemical reaction. The symmetrical distribution of the surface map of the HE generation rate for UP excitation (Figure 2e) supports the expectation of an achiral growth under such conditions. Simultaneously, the HE surface maps show asymmetries for both types of CPL illumination (Figure 2f and g), which should lead to the HE-induced growth of chiral particles. The asymmetry between the two maps (LCP and RCP) is clear but subtle. The differential (i.e., CD) HE rates map, displayed in Figure 2h, more explicitly reveals the spatial origins of a seed-like

growth of chiral patterns promoted by the HEs. This illustrates the spatial differentiation beginning with achiral NCs, which illuminated with opposite polarizations of CPL, leads to a small initial asymmetric growth that can be amplified through continued excitation and material deposition.

### Chiral Evolution of Au Nanostructures

To further elucidate the mechanism of chirality transfer from the CPL to the NCs on substrates, we acquired correlated SEM images and CDS spectra at various time-evolution stages. After 1 min of RCP illumination (Figure 3a), some Au<sup>3+</sup> ions were already reduced to Au<sup>0</sup>, and small clusters grew locally in the hot-spot areas near the vertices and edges of AuNCs, where the strongly localized HEs could proceed with the plasmon-driven chemical reactions (Figure 2f). Upon prolonged illumination, the AuNCs grew into more intricate shapes (Figure 3b and c) due to the varying optical properties during the cluster formation and nanoparticle growth. This unique chiral growth differs from previously reported chiral growth of semiconductor PbO<sub>2</sub> on Au nanocuboids.<sup>[43–44]</sup> Typically, the lattice mismatch between metals and semiconductors with distinct lattice constants presents an obstacle to epitaxial growth.<sup>[57]</sup> In our growth system with just one type of metal, there is no lattice mismatch for the growth, enabling the growth of nanoparticles to follow well the chirally distributed HEs on their surfaces. While the area around the edges

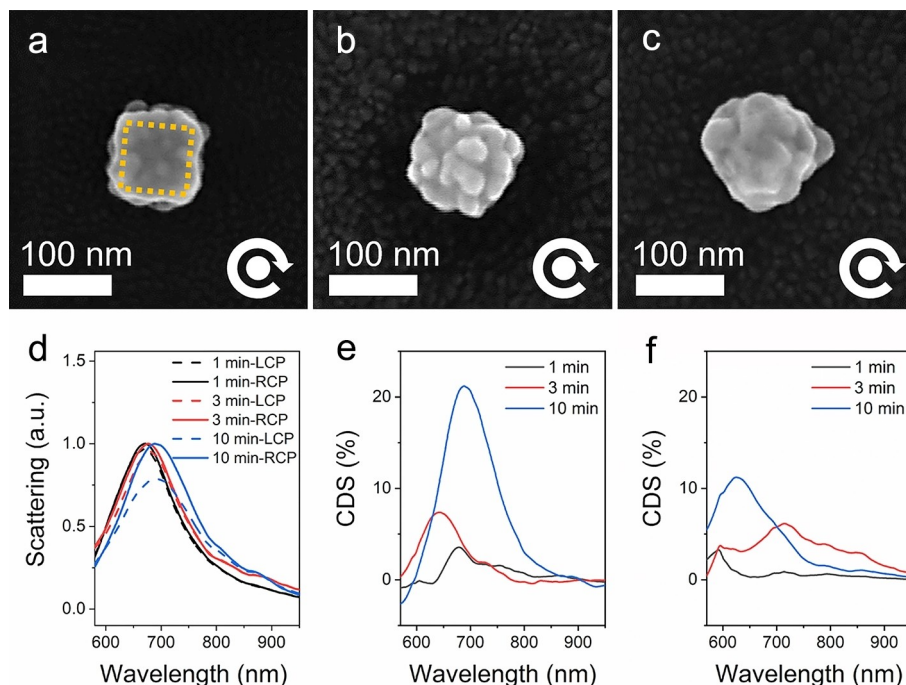


**Figure 3.** Time-dependent plasmon-induced chiral growth of AuNCs. Representative SEM images of RAuNCs collected at different reaction times during RCP illumination for (a) 1 min, (b) 3 min, and (c) 10 min. The overlaid orange square indicates a 75 nm-sized AuNC. (d) The corresponding normalized scattering spectra for 1 min (black), 3 min (red), and 10 min (blue) from single-particle scattering experiments. Time evolution of the CDS spectra of RAuNCs at each growth time (e) at the single-particle and (f) ensemble levels.

and vertices is small compared to the overall area, the HE generation rate there is high. In contrast, the area of the facets is much larger, but the HE generation rate is relatively low. This leads to a differentiated picture for the plasmon-induced chemical reaction rates of material deposition over the entire NC surface. Consequently, these varying growth rates at the edges, vertices, and facets of the AuNCs can result in complex shapes of the final chiral nanostructures. To ascertain that each NC retains its intrinsic chirality during nanoparticle growth through plasmon-driven chemical reactions, we measured the single-particle scattering spectra and calculated their respective CDS. As the illumination time increased, the LSPR peak of each RAuNC was red-shifted to 671 nm (1 min), 677 nm (3 min), and 688 nm (10 min), compared to the initial AuNC peak at 590 nm (Figure 3d). This phenomenon can be mainly attributed to the increase in nanoparticle size, leading to the red-shifted LSPR peak position.<sup>[57]</sup> Additionally, the single-particle and ensemble CDS intensity increased and maintained a positive CDS signal during the RCP-plasmon-induced chiral growth (Figure 3e and f). These time evolution-supported findings indicate how the chirality transfer through plasmon-driven chemical reactions occurred in our system. We propose that the reduction of Au ions occurs through the involvement of HEs generated on the surface of the AuNCs during CPL illumination. To further confirm the mediation of HEs in the localized growth process, we proceeded with the reactions by varying the power of CPL illumination (Figure S10). The prepared RAuNC with a power density of 141  $\mu\text{W}/\text{cm}^2$  illumination, which is a lower power density compared to its counterpart under 846  $\mu\text{W}/\text{cm}^2$ , shows a much smaller size as well as smaller clusters on the surface of nanocubes. The lower intensity of CPL illumination results in less HEs generation, which in turn reduces the chiral growth on achiral AuNCs. Under dark conditions, negligible growth of nanoparticles was observed on the surface of the AuNCs due to the absence of reducing agents in our reaction system (Figure S11a and b). In the absence of a hole scavenger in the solution, we observed significantly less nanoparticle growth compared to the conditions where a hole scavenger was present (Figure S11c). From these results, we deduce that HEs indeed predominantly mediate the localized growth on the AuNCs. These HEs could further induce the chirality transfer from light to matter through plasmon-driven chemical reactions.

The photothermal and hot-carrier mechanisms have sparked numerous debates in the field of plasmonic-assisted photocatalysis,<sup>[58–60]</sup> however, in our system, such observable site-selective growth of Au on the AuNCs serves as additional evidence for the HE-mediated mechanism. Because of the high thermal conductivity of metals, heat transfer by free electrons inside metals has priority over phonon-assisted flow via surface-adsorbed molecules. We thus expect that photothermal heat effects on the surface of the AuNCs play a subordinate role in the chiral material deposition.<sup>[61]</sup> Even if some reactions were heat-induced, the heat would quickly delocalize and the reactions would occur

homogeneously on the surfaces of the AuNCs, which cannot explain the localized growth we observed.

### Effect of Wavelength on Chiral Evolution

To further clarify the role of hot-electron generation in plasmon-induced chirality transfer, we prepared 100 nm-sized AuNCs. This size of AuNC, compared to 75 nm, enables the selection of a scattering- or absorption-dominated excitation regime depending on the incident wavelength (Figure 4a and Figure S12). This prompted us to study the wavelength dependence of chirality transfer related to potential differences in HE generation. We conducted plasmon-induced growth of the 100 nm AuNCs at 565 nm and 640 nm. Interestingly, we indeed observed a difference in hot electron-mediated growth depending on the incident wavelength. When illuminated at 565 nm, the size of the chiral Au nanostructures was larger than those illuminated with 640 nm (Figure 4b and c). Furthermore, the scattering peak position was red-shifted for RCP illumination with 565 nm compared to 640 nm (Figure 4d). Also here, the CDS spectra of each nanostructure clearly showed positive CDS signals in both single-particle and ensemble CDS measurements (Figure 4e and f). These results indicate that plasmon-induced chirality transfer occurs in a wavelength-dependent manner and that absorption is the dominant pathway. We calculated HE mapping images of AuNC under CPL with 565 nm and 640 nm (Figure 4g). Chiral-distributed HEs were clearly observed on the surface of AuNCs under CPL illumination at both wavelengths, driving the plasmon-induced chiral growth. The HE generation rate under 565 nm illumination was found to be twice that under 640 nm (Figure 4h), which explains the larger chiral growth under 565 nm compared to that under 640 nm. Furthermore, we computed the optical properties of the RAuNC model that is built upon a theoretical methodology of photo-growth processes in our previous work<sup>42</sup> and reflects the geometry of RAuNC after growth (Figure 4i). The computed normalized scattering and CDS cross sections of chiral RAuNC and achiral AuNC are depicted in Figure 4j and k. Compared with achiral AuNC, the chiral RAuNC shows a red-shift in the scattering and exhibits clear chiroptical behavior, which is in good agreement with the experimental results.

### Plasmon-induced chirality transfer in the bimetallic system

To assess the feasibility of plasmon-induced chirality transfer across various metal growth systems, we conducted chiral growth experiments on AuNCs using silver and palladium precursors ( $\text{AgNO}_3$  and  $\text{K}_2\text{PdCl}_4$ ). The chiral characteristics of the NPs synthesized by  $\text{AgNO}_3$  (Ag-RAuNCs) and  $\text{K}_2\text{PdCl}_4$  (Pd-RAuNCs) under RCP illumination for 20 min were investigated by SEM and single-particle CDS scattering measurement. Interestingly, we observed a successful chirality transfer between different metals. Both Ag-RAuNCs and Pd-RAuNCs exhibited more growth on one side of the vertices, thereby breaking mirror symmetry and

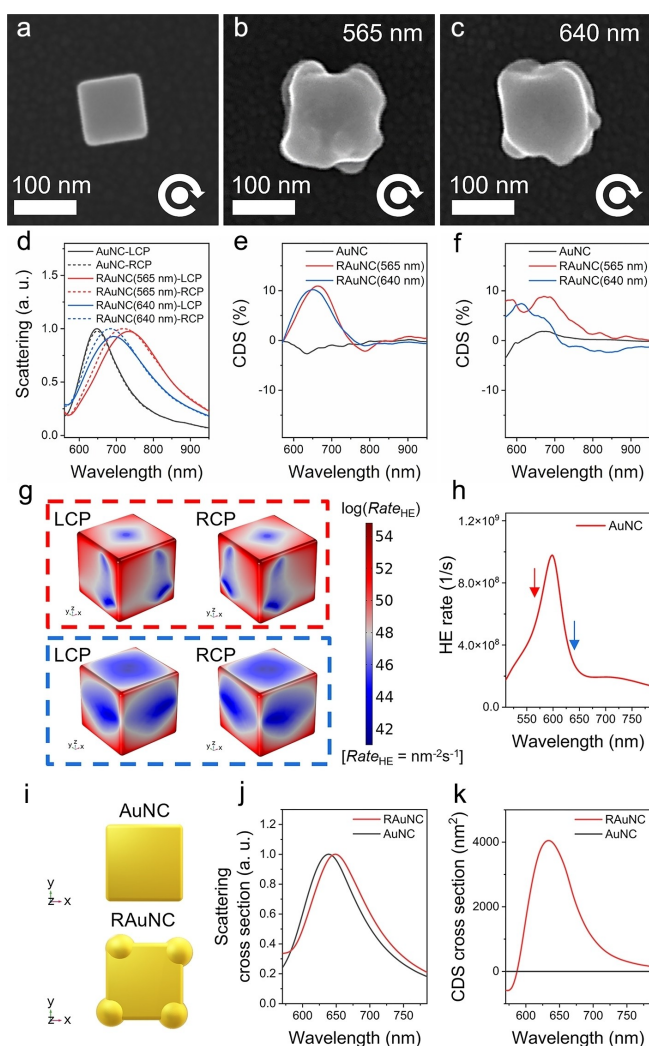


**Figure 4.** Wavelength-dependent plasmon-induced chiral growth of AuNCs. SEM images of (a) a 100 nm-sized AuNC seed, and RAuNCs after growth under RCP illumination at (b) 565 nm and (c) 640 nm. (d) Single-particle scattering spectra of RAuNCs under RCP light illumination at 565 nm and 640 nm. (e) Corresponding single-particle CDS spectra of each NC displayed in (b) and (c). (f) Ensemble CDS spectra of each NC shown in (b) and (c). (g) HE mapping images of a model AuNC seed under LCP and RCP light illumination at 565 nm (red) and 640 nm (blue). (h) HE generation rate for the AuNC seed. (i) Chiral RAuNC and achiral AuNC models for theoretical simulations. (j) Computed normalized scattering cross sections for the chiral RAuNC and achiral AuNC. (k) Computed CDS cross sections for RAuNC and AuNC.

generating chirality (Figure 5a and b). The single-particle scattering spectra (Figure 5c) show the LSPR peaks of these chiral nanostructures were red-shifted to 607 nm (Pd-RAuNCs) and 624 nm (Ag-RAuNCs), compared to the original 75-nm AuNCs with 590 nm. Pd-RAuNCs and Ag-RAuNCs both exhibited positive CDS signals following the growth induced by RCP light, and the more asymmetric shape of Pd-RAuNCs also resulted in higher CDS values compared to Ag-RAuNCs (Figure 5d).

Notably, each bimetallic growth system shows different chiral growth compared to the Au monometallic growth

system. The localized chiral growth of Ag on AuNCs (Figure 5a) predominantly occurred at the vertices and edges, recognized as hot-spot areas of AuNCs. However, the 20-min Ag chiral growth was less compared to its Au counterpart (Figure 1c), resulting in the nanoparticle at an early growth stage, similar to the 1-min RAuNC (Figure 3a). In contrast, Pd exhibited selective growth near the vertices, forming large Pd nanoparticles. These diverse growth trends observed in bimetallic systems during the plasmon-induced chemical reaction could arise from the different reduction potentials of each precursor. The reduction potential of  $[\text{AuCl}_4]^-/\text{Au}$  pair (1.00 V versus RHE) is higher than  $\text{Ag}^+/\text{Ag}$  pair (0.80 V versus RHE) and  $[\text{PdCl}_4]^{2-}/\text{Pd}$  pair (0.62 V versus RHE),<sup>[62–63]</sup> so the chiral growth of Ag and Pd on AuNCs is hard and requires hot electrons with higher energy compared to that of Au on AuNCs. To verify this point, we added excess NaBr to the  $\text{HAuCl}_4$  precursor to replace the ligands of  $[\text{AuCl}_4]^-$  and form  $[\text{AuBr}_4]^-$ , which is chemically more stable than  $[\text{AuCl}_4]^-$  with lower reduction potential ( $[\text{AuBr}_4]^-/\text{Au}$  pair, 0.85 V versus RHE).<sup>[64]</sup> After performing the plasmon-induced chiral growth with  $[\text{AuBr}_4]^-$ , we obtained very similar results to those for Ag-RAuNCs (Figure S13). For Pd-RAuNCs, the morphology could come not only from the low reduction potential of the precursor but also from the lattice mismatch between Au and Pd. Due to the different lattice constants of Au and Pd (407 pm and 389 pm, respectively), Pd tends to grow more on its own surface rather than on Au. Meanwhile Ag, with a similar lattice constant (408 pm) to Au, exhibits growth trends similar to that of Au.<sup>[63,65]</sup> Overall, the plasmon-induced chirality transfer mechanism is also adapted to the growth of other metals. However, further research is required to achieve more asymmetric chiral nanostructures with higher chiroptical responses by optimizing the synthetic parameters of our hot-electron mediated chiral growth.

## Conclusions

In summary, we have described a systematic investigation of the plasmon-driven growth of chiral nanoparticles, achieved through chirality transfer from CPL without the need for chiral molecules. The chiroptical properties of the synthesized chiral AuNCs were characterized using both ensemble and single-particle CDS measurements, providing evidence of their intrinsic chirality. The experimental observation of plasmon-induced chirality transfer was supported by theoretical simulations based on the generation of chirally distributed HEs resulting from the interaction between CPL and achiral AuNCs. The chirally distributed HEs can induce chirality transfer via light-matter interactions (i.e., localized reduction of the Au precursor), leading to the formation of chiral nanostructures. Moreover, this work provides further insights into the synthesis of hybrid chiral nanomaterials, like Ag-Au and Pd-Au, based on the plasmon-induced chirality transfer mechanism. We believe this work sheds light on the emergence of chirality transfer and will have significant implications in various fields, including asymmet-

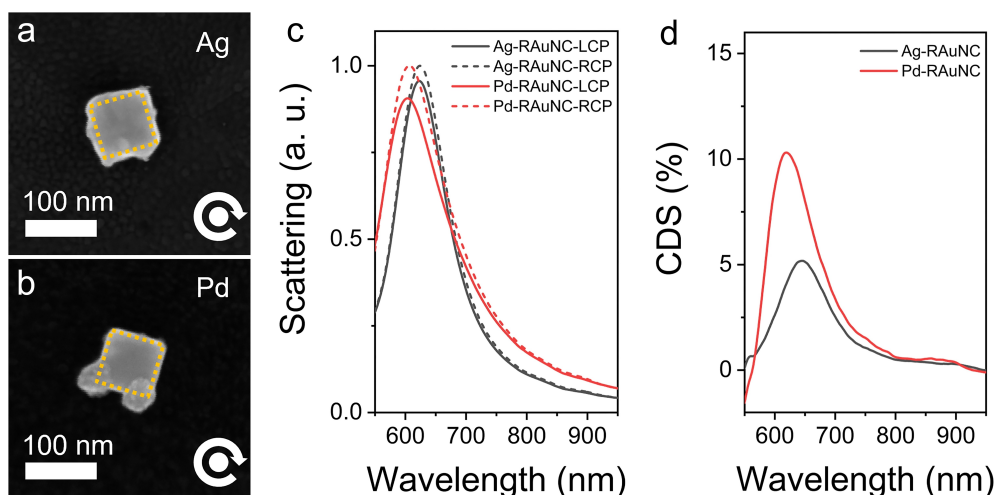


**Figure 5.** Chiral growth of Ag and Pd on AuNCs. Representative SEM images of RAuNCs grown with (a) Ag and (b) Pd under RCP illumination. The overlaid orange square indicates a 75 nm-sized AuNC. (c) The corresponding normalized single-particle scattering spectra and (d) CDS spectra of Ag-RAuNC (black) and Pd-RAuNC (red).

ric synthesis, chiral catalysis, chiral metasurfaces, and chirality sensing.

### Acknowledgements

This work was supported by the Deutsche Forschungsgemeinschaft (DFG, German Research Foundation) under Germany's Excellence Strategy – EXC 2089/1 – 390776260, the Bavarian program Solar Energies Go Hybrid (SolTech), the Center for NanoScience (CeNS) and the European Commission through the ERC Starting Grant CATALIGHT (802989). S. L. acknowledges funding and support from the National Research Foundation of Korea (NRF) grant funded by the Korea government (MSIT) (NRF-2022R1C1C1005381). A.M. acknowledges the National Natural Science Foundation of China (Grant number 12250410256). H.R. acknowledges the funding support from the Australian Research Council (DECRA Project DE220101085). L.V.B. acknowledges the support from the Spanish Ministerio de Ciencia e Innovación through a Ramón y Cajal fellowship (RYC2021-033818-I) and under projects PID2020-118282RA-I00 and TED2021-130038A-I00. Open Access funding enabled and organized by Projekt DEAL.

### Conflict of Interest

The authors declare no conflict of interest.

### Data Availability Statement

The data that support the findings of this study are available from the corresponding author upon reasonable request.

**Keywords:** chirality transfer · hot electrons · metal nanoparticles · plasmonics · single-particle scattering

- [1] A. Salam, *J. Mol. Evol.* **1991**, *33*, 105–113.
- [2] F. Zaera, *Chem. Soc. Rev.* **2017**, *46*, 7374–7398.
- [3] D. P. Glavin, A. S. Burton, J. E. Elsil, J. C. Aponte, J. P. Dworkin, *Chem. Rev.* **2019**, *120*, 4660–4689.
- [4] L. A. Warning, A. R. Miandashti, L. A. McCarthy, Q. Zhang, C. F. Landes, S. Link, *ACS Nano* **2021**, *15*, 15538–15566.
- [5] S. Adhikari, M. Orrit, *ACS Photonics* **2022**, *9*, 3486–3497.
- [6] J. Karst, N. H. Cho, H. Kim, H.-E. Lee, K. T. Nam, H. Giessen, M. Hentschel, *ACS Nano* **2019**, *13*, 8659–8668.
- [7] J. Kumar, L. M. Liz-Marzán, *Bull. Chem. Soc. Jpn.* **2019**, *92*, 30–37.
- [8] M. L. Solomon, A. A. Saleh, L. V. Poulikakos, J. M. Abendroth, L. F. Tadesse, J. A. Dionne, *Acc. Chem. Res.* **2020**, *53*, 588–598.
- [9] J. Pendry, *Science* **2004**, *306*, 1353–1355.
- [10] M. Thiel, M. S. Rill, G. Von Freymann, M. Wegener, *Adv. Mater.* **2009**, *21*, 4680–4682.
- [11] K. W. Smith, S. Link, W.-S. Chang, *J. Photochem. Photobiol. C* **2017**, *32*, 40–57.
- [12] Q. Zhang, T. Hernandez, K. W. Smith, S. A. Hosseini Jebeli, A. X. Dai, L. Warning, R. Baiyasi, L. A. McCarthy, H. Guo, D. H. Chen, J. A. Dionne, C. F. Landes, S. Link, *Science* **2019**, *365*, 1475–1478.
- [13] Y. Negrín-Montecelo, A. Movsesyan, J. Gao, S. Burger, Z. M. Wang, S. Nlate, E. Pouget, R. Oda, M. Comesaña-Hermo, A. O. Govorov, M. A. Correa-Duarte, *J. Am. Chem. Soc.* **2022**, *144*, 1663–1671.
- [14] F. Wu, Y. Tian, X. Luan, X. Lv, F. Li, G. Xu, W. Niu, *Nano Lett.* **2022**, *22*, 2915–2922.
- [15] C. Hao, L. Xu, W. Ma, X. Wu, L. Wang, H. Kuang, C. Xu, *Adv. Funct. Mater.* **2015**, *25*, 5816–5822.
- [16] X. Sun, H. Kong, Q. Zhou, S. Tsunega, X. Liu, H. Yang, R.-H. Jin, *Anal. Chem.* **2020**, *92*, 8015–8020.
- [17] Z. Liu, J. Ai, P. Kumar, E. You, X. Zhou, X. Liu, Z. Tian, P. Bour, Y. Duan, L. Han, N. A. Kotov, S. Ding, S. Che, *Angew. Chem. Int. Ed.* **2020**, *59*, 15226–15231.
- [18] S. X. Leong, C. S. L. Koh, H. Y. F. Sim, Y. H. Lee, X. Han, G. C. Phan-Quang, X. Y. Ling, *ACS Nano* **2021**, *15*, 1817–1825.



- [19] L. Xu, X. Wang, W. Wang, M. Sun, W. J. Choi, J. Y. Kim, C. Hao, S. Li, A. Qu, M. Lu, X. Wu, F. M. Colombari, W. R. Gomes, A. L. Blanco, A. F. de Moura, X. Guo, H. Kuang, N. A. Kotov, C. Xu, *Nature* **2022**, *601*, 366–373.
- [20] J. Kumar, H. Eraña, E. López-Martínez, N. Claes, V. F. Martín, D. M. Solís, S. Bals, A. L. Cortajarena, J. Castilla, L. M. Liz-Marzán, *Proc. Natl. Acad. Sci. USA* **2018**, *115*, 3225–3230.
- [21] N.-N. Zhang, H.-R. Sun, S. Liu, Y.-C. Xing, J. Lu, F. Peng, C.-L. Han, Z. Wei, T. Sun, B. Yang, *CCS Chemistry* **2022**, *4*, 660–670.
- [22] E. Hendry, T. Carpy, J. Johnston, M. Popland, R. Mikhaylovskiy, A. Laphorn, S. Kelly, L. Barron, N. Gadegaard, M. Kadodwala, *Nat. Nanotechnol.* **2010**, *5*, 783–787.
- [23] G. Wang, C. Hao, W. Ma, A. Qu, C. Chen, J. Xu, C. Xu, H. Kuang, L. Xu, *Adv. Mater.* **2021**, *33*, 2102337.
- [24] Z. Cao, H. Gao, M. Qiu, W. Jin, S. Deng, K. Y. Wong, D. Lei, *Adv. Mater.* **2020**, *32*, 1907151.
- [25] J. Lu, Y. Xue, K. Bernardino, N. N. Zhang, W. R. Gomes, N. S. Ramesar, S. Liu, Z. Hu, T. Sun, A. F. De Moura, N. A. Kotov, K. Liu, *Science* **2021**, *371*, 1368–1374.
- [26] R. M. Kim, J. H. Huh, S. Yoo, T. G. Kim, C. Kim, H. Kim, J. H. Han, N. H. Cho, Y. C. Lim, S. W. Im, E. Im, J. R. Jeong, M. H. Lee, T. Y. Yoon, H. Y. Lee, Q. H. Park, S. Lee, K. T. Nam, *Nature* **2022**, *612*, 470–476.
- [27] Y. Zhong, T. J. Sisto, B. Zhang, K. Miyata, X.-Y. Zhu, M. L. Steigerwald, F. Ng, C. Nuckolls, *J. Am. Chem. Soc.* **2017**, *139*, 5644–5647.
- [28] H. Zhang, A. O. Govorov, *Phys. Rev. B* **2013**, *87*, 075410.
- [29] B. M. Maoz, Y. Chaikin, A. B. Tesler, O. Bar Elli, Z. Fan, A. O. Govorov, G. Markovich, *Nano Lett.* **2013**, *13*, 1203–1209.
- [30] J. M. Slocik, A. O. Govorov, R. R. Naik, *Nano Lett.* **2011**, *11*, 701–705.
- [31] A. O. Govorov, Z. Fan, P. Hernandez, J. M. Slocik, R. R. Naik, *Nano Lett.* **2010**, *10*, 1374–1382.
- [32] A. Kuzyk, R. Schreiber, Z. Fan, G. Pardatscher, E.-M. Roller, A. Högele, F. C. Simmel, A. O. Govorov, T. Liedl, *Nature* **2012**, *483*, 311–314.
- [33] X. Lan, X. Lu, C. Shen, Y. Ke, W. Ni, Q. Wang, *J. Am. Chem. Soc.* **2015**, *137*, 457–462.
- [34] J. George, K. G. Thomas, *J. Am. Chem. Soc.* **2010**, *132*, 2502–2503.
- [35] H.-E. Lee, H.-Y. Ahn, J. Mun, Y. Y. Lee, M. Kim, N. H. Cho, K. Chang, W. S. Kim, J. Rho, K. T. Nam, *Nature* **2018**, *556*, 360–365.
- [36] J. Majoinen, J. Hassinen, J. S. Haataja, H. T. Rekola, E. Kontturi, M. A. Kostianen, R. H. Ras, P. Törmä, O. Ikkala, *Adv. Mater.* **2016**, *28*, 5262–5267.
- [37] G. Gonzalez-Rubio, J. Mosquera, V. Kumar, A. Pedrazo-Tardajos, P. Llombart, D. M. Solis, I. Lobato, E. G. Noya, A. Guerrero-Martinez, J. M. Taboada, F. Obelleiro, L. G. MacDowell, S. Bals, L. M. Liz-Marzán, *Science* **2020**, *368*, 1472–1477.
- [38] J.-Y. Kim, J. Yeom, G. Zhao, H. Calcaterra, J. Munn, P. Zhang, N. Kotov, *J. Am. Chem. Soc.* **2019**, *141*, 11739–11744.
- [39] K. Saito, T. Tatsuma, *Nano Lett.* **2018**, *18*, 3209–3212.
- [40] H. Wang, Y. Liu, J. Yu, Y. Luo, L. Wang, T. Yang, B. Raktani, H. Lee, *ACS Appl. Mater. Interfaces* **2022**, *14*, 3559–3567.
- [41] X. Wei, J. Liu, G.-J. Xia, J. Deng, P. Sun, J. J. Chruma, W. Wu, C. Yang, Y.-G. Wang, Z. Huang, *Nat. Chem.* **2020**, *12*, 551–559.
- [42] L. V. Besteiro, A. Movsesyan, O. Ávalos-Ovando, S. Lee, E. Cortés, M. A. Correa-Duarte, Z. M. Wang, A. O. Govorov, *Nano Lett.* **2021**, *21*, 10315–10324.
- [43] J.-E. Park, Y. Lee, J.-M. Nam, *Nano Lett.* **2018**, *18*, 6475–6482.
- [44] T. Yuthalekha, C. Wattanakit, V. Lapeyre, S. Nokbin, C. Warakulwit, J. Limtrakul, A. Kuhn, *Nat. Commun.* **2016**, *7*, 12678.
- [45] X. Lv, F. Wu, Y. Tian, P. Zuo, F. Li, G. Xu, W. Niu, *Adv. Mater.* **2023**, 2305429.
- [46] Y. Negrin-Montecelo, A. Movsesyan, J. Gao, S. Burger, Z. M. Wang, S. Nlate, E. Pouget, R. Oda, M. Comesana-Hermo, A. O. Govorov, M. A. Correa-Duarte, *J. Am. Chem. Soc.* **2022**, *144*, 1663–1671.
- [47] S. D. Golze, R. A. Hughes, S. Rouvimov, R. D. Neal, T. B. Demille, S. Neretina, *Nano Lett.* **2019**, *19*, 5653–5660.
- [48] Y. Zhai, J. S. DuChene, Y. C. Wang, J. Qiu, A. C. Johnston-Peck, B. You, W. Guo, B. DiCiccio, K. Qian, E. W. Zhao, F. Ooi, D. Hu, D. Su, E. A. Stach, Z. Zhu, W. D. Wei, *Nat. Mater.* **2016**, *15*, 889–895.
- [49] L. K. Khorashad, L. V. Besteiro, M. A. Correa-Duarte, S. Burger, Z. M. Wang, A. O. Govorov, *J. Am. Chem. Soc.* **2020**, *142*, 4193–4205.
- [50] P. Spaeth, S. Adhikari, L. Le, T. Jollans, S. Pud, W. Albrecht, T. Bauer, M. Caldarola, L. Kuipers, M. Orrit, *Nano Lett.* **2019**, *19*, 8934–8940.
- [51] P. Spaeth, S. Adhikari, M. D. Baaske, S. Pud, J. Ton, M. Orrit, *ACS Nano* **2021**, *15*, 16277–16285.
- [52] A. Rafiei Miandashti, L. Khosravi Khorashad, M. E. Kordesch, A. O. Govorov, H. H. Richardson, *ACS Nano* **2020**, *14*, 4188–4195.
- [53] E. Vinegrad, D. Vestler, A. Ben-Moshe, A. R. Barnea, G. Markovich, O. Cheshnovsky, *ACS Photonics* **2018**, *5*, 2151–2159.
- [54] S. Link, M. A. El-Sayed, *J. Phys. Chem. B* **1999**, *103*, 4212–4217.
- [55] P. K. Jain, M. A. El-Sayed, *Nano Lett.* **2008**, *8*, 4347–4352.
- [56] A. Movsesyan, A. Muravitskaya, L. V. Besteiro, E. Y. Santiago, O. Ávalos-Ovando, M. A. Correa-Duarte, Z. Wang, G. Markovich, A. O. Govorov, *Adv. Opt. Mater.* **2023**, 2300013.
- [57] C. L. Nehl, J. H. Hafner, *J. Mater. Chem.* **2008**, *18*, 2415–2419.
- [58] R. C. Elias, S. Linic, *J. Am. Chem. Soc.* **2022**, *144*, 19990–19998.
- [59] Y. Dubi, Y. Sivan, *Light-Sci. Appl.* **2019**, *8*, 89.
- [60] Y. Dubi, I. W. Un, Y. Sivan, *Chem. Sci.* **2020**, *11*, 5017–5027.
- [61] C. Kittel, *Introduction to solid state physics*, Wiley, **2005**.
- [62] H. Zhang, M. Jin, J. Wang, W. Li, P. H. Camargo, M. J. Kim, D. Yang, Z. Xie, Y. Xia, *J. Am. Chem. Soc.* **2011**, *133*, 6078–6089.
- [63] Y. Sun, Y. Xia, *J. Am. Chem. Soc.* **2004**, *126*, 3892–3901.
- [64] X. Qiu, V. Pawlik, S. Zhou, J. Tao, Y. Xia, *J. Am. Chem. Soc.* **2023**, *145*, 13400–13410.
- [65] Y. Ding, F. Fan, Z. Tian, Z. L. Wang, *J. Am. Chem. Soc.* **2010**, *132*, 12480–12486.

Manuscript received: December 22, 2023

Accepted manuscript online: January 18, 2024

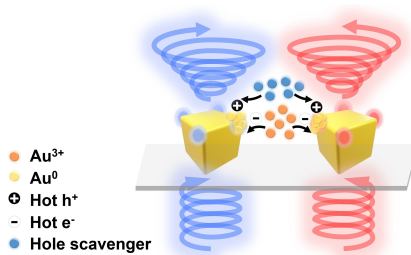
Version of record online: ■■■, ■■■

## Research Articles

## Chirality Transfer

S. Lee,\* C. Fan, A. Movsesyan, J. Bürger,  
F. J. Wendisch, L. de S. Menezes,  
S. A. Maier, H. Ren, T. Liedl, L. V. Besteiro,  
A. O. Govorov,\* E. Cortés\* — e202319920

Unraveling the Chirality Transfer from Circularly Polarized Light to Single Plasmonic Nanoparticles



The chirality transfer from light to matter was explored by proceeding with the plasmon-driven chemical reaction involving chirally distributed hot electrons with achiral Au nanoparticles and circularly polarized light. The chiral light-matter interactions were unraveled by circular differential scattering spectroscopy at the single particle level and theoretical simulations.